ELSEVIER

Nuclear Physics A 597 (1996) 231-252

NUCLEAR
PHYSICS A

# Determination of $\alpha$-widths in $^{19}$F relevant to fluorine nucleosynthesis

F. de Oliveira[a], A. Coc[a], P. Aguer[a], C. Angulo[a], G. Bogaert[a],
J. Kiener[a], A. Lefebvre[a], V. Tatischeff[a], J.-P. Thibaud[a], S. Fortier[b],
J.M. Maison[b], L. Rosier[b], G. Rotbard[b], J. Vernotte[b], M. Arnould[c],
A. Jorissen[c], N. Mowlavi[c]

[a] *CSNSM, IN2P3-CNRS, 91405 Orsay Campus, France*
[b] *IPN, IN2P3-CNRS et Université de Paris-Sud, 91406 Orsay Cedex, France*
[c] *Institut d'Astronomie et d'Astrophysique, ULB, Campus Plaine, CP226, Bd. du Triomphe, B-1050 Bruxelles, Belgium*

Received 20 July 1995

---

## Abstract

Nucleosynthesis of fluorine in the context of helium burning occurs through the $^{15}$N$(\alpha,\gamma)^{19}$F reaction. At temperatures where fluorine formation takes place in most astrophysical models, the narrow resonance associated with the 4.378 MeV level of $^{19}$F is expected to dominate the reaction rate, but its strength is not known. We used a $^{15}$N confined gas target to study this level by means of the transfer reaction $^{15}$N$(^{7}$Li,t$)^{19}$F at 28 MeV. Reaction products were analysed with a split pole magnetic spectrometer and the angular distributions for the first 16 levels of $^{19}$F were extracted. These distributions are fairly well reproduced by FR-DWBA calculations in the framework of an $\alpha$-cluster transfer model with a compound-nucleus contribution obtained by Hauser–Feshbach calculations. $\alpha$-spectroscopic factors were deduced and, for unbound levels, the $\alpha$-widths were determined and compared with the existing direct measurements. The $\alpha$-width of the level of astrophysical interest ($E_x$ = 4.378 MeV) was found to be $\Gamma_\alpha = 1.5 \times 10^{-9}$ eV, a value 60 times smaller than the commonly used one. The astrophysical consequences for $^{19}$F production in AGB stars are discussed.

*Keywords:* Nuclear reactions $^{19}$F $^{19}$Ne $^{15}$N$(\alpha,\gamma)$, $^{15}$N$(^{7}$Li,t$)$, $E = 28$ MeV, enriched gas target; spectroscopic factors; astrophysical reaction rate; FR-DWBA analysis; Hauser–Feshbach contribution; $\alpha$-transfer reactions; cluster model; deduced $\alpha$-widths; AGB stars; $^{19}$F nucleosynthesis

---

*SSDI* 0375-9474(95)00455-6

## 1. Introduction

Despite large theoretical and experimental efforts, the nucleosynthetic origin of fluorine is not clearly understood and several astrophysical sites have been suggested for its production [1]. Explosive hydrogen burning in novae has sometimes been presented as a possible site for $^{19}$F production [2]. Recent calculations [3,4] indicate that some $^{19}$F can indeed be produced in such conditions, through the chain

$$^{16}\mathrm{O}(\mathrm{p},\gamma)^{17}\mathrm{F}(\beta^+)^{17}\mathrm{O}(\mathrm{p},\gamma)^{18}\mathrm{F}(\mathrm{p},\gamma)^{19}\mathrm{Ne}(\beta^+)^{19}\mathrm{F},$$

however, it does not represent a significant contribution to the enrichment of the interstellar medium (ISM) in $^{19}$F. Another scenario predicts that the inelastic scattering on $^{20}$Ne of neutrinos produced in the core of a Type II supernova could be responsible for a sizeable fraction of the galactic $^{19}$F content [5-7]. The expected level of production depends in fact critically on the uncertain high-energy tail of the supernova neutrino spectrum. Helium-burning environments have also been identified as promising sites for $^{19}$F production. A type of Wolf-Rayet stars has been pointed out as substantial contributors to the ISM enrichment in $^{19}$F [8]. Fluorine can also be produced during thermal pulses in asymptotic giant branch (AGB) stars [9], and brought to the surface by the so-called "third dredge-up". Large overabundances of fluorine (up to 30 times solar) have indeed been detected in the envelope of AGB stars from the observation of infrared rotation-vibration lines of the HF molecule [10]. These observations suggest that the He-burning shell of AGB stars is an important site of fluorine production [9]. In this context, the reaction $^{15}\mathrm{N}(\alpha,\gamma)^{19}\mathrm{F}$ plays a key role. The chain $^{14}\mathrm{N}(\alpha,\gamma)^{18}\mathrm{F}(\beta^+)^{18}\mathrm{O}(\mathrm{p},\alpha)^{15}\mathrm{N}(\alpha,\gamma)^{19}\mathrm{F}$ operating on $^{14}$N left over from the former operation of the CNO cycles is in fact responsible for the $^{19}$F synthesis in He-burning environments, with protons coming from ($\alpha$,n) followed by (n,p) reactions (Section 5). The astrophysical $^{15}\mathrm{N}(\alpha,\gamma)^{19}\mathrm{F}$ reaction rate is not well known, in particular in the relevant temperature range. In their last compilation, Caughlan and Fowler [11], quoted CF88 in the following, used three terms for the reaction rate (Fig. 1), a non-resonant term at low temperature, a term for the narrow resonance corresponding to the level at 4.378 MeV in $^{19}$F and a continuum term at high temperature. For temperatures below $T_9 = 0.5$ (with the usual notation $T_x = A$ meaning $T = A \times 10^x$), at which $^{19}$F formation takes place in most models, the resonance at $E_x = 4.378$ MeV (Fig. 2) has the highest contribution. The value used for the resonance in CF88 comes from the crude estimate of an $\alpha$-width equal to 10% of the Wigner limit ($\theta^2 = 0.1$).

A direct measurement seems unworkable, owing to the very weak cross section. As the resonance is narrow, isolated and its $\gamma$-width is much higher than its $\alpha$-width [12], the reaction rate is just proportional to the $\alpha$-width. As the determination of an $\alpha$ transfer spectroscopic factor could allow a better estimate of the $\alpha$-width, we have studied the $^{15}\mathrm{N}(^7\mathrm{Li},\mathrm{t})^{19}\mathrm{F}$ reaction. This reaction has been studied previously [13] at 15 MeV and the angular distributions for the low-lying negative parity states were analysed by DWBA [14] but no spectroscopic factor was given for the weakly populated level of astrophysical interest. We measured the angular distributions corresponding to the first

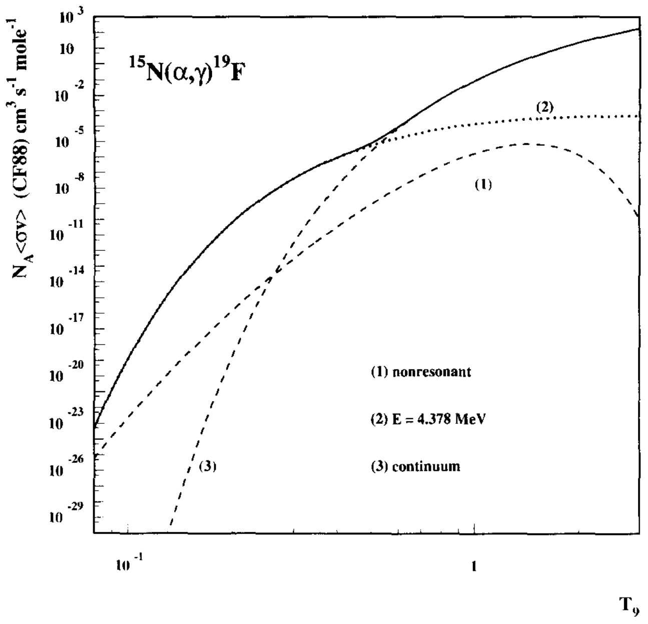

Fig. 1. The CF88 reaction rate is divided into 3 parts: the non-resonant part (1), the resonant part (2) associated with the 4.378 MeV level and the continuum part (3). The sum of these contributions is represented by the solid line. $T_9$ is the temperature in billion degrees.

16 levels of $^{19}F$, including the level of astrophysical importance at $E_x$ = 4.378 MeV, and analysed them by FR-DWBA to extract $\alpha$-widths.

In Section 2 we present the experimental method, data analysis and results for the elastic scattering reaction $^{15}N(^7Li,^7Li)^{15}N$ cross section and the $^{15}N(^7Li,t)^{19}F$ transfer reaction. In Section 3 the results of DWBA analysis are discussed and specifically the sensitivity to the parameters. Spectroscopic factors and $\alpha$-widths are determined for many $^{19}F$ levels. Section 4 presents the new $^{15}N(\alpha,\gamma)^{19}F$ rate and Section 5 the astrophysical consequences for $^{19}F$ production in AGB stars. Details on this experiment and subsequent analysis can be found in Ref. [15].

## 2. Experimental method

### 2.1. Experimental set-up and spectra analysis

Previous experiments have shown that solid targets such as melamine ($C_3H_6N_6$) could not be used due to the large carbon contamination of the spectra preventing the measurement of angular distributions. So we used for this experiment a $^{15}N$ confined gas target (enriched to 99%) with a pressure close to 100 mbar. The experiment was carried out with a 28 MeV $^7Li^{+++}$ beam from the Orsay Institut de Physique Nucléaire Tandem accelerator. The beam entered and emerged from the cell through thin (0.6 $\mu$m,

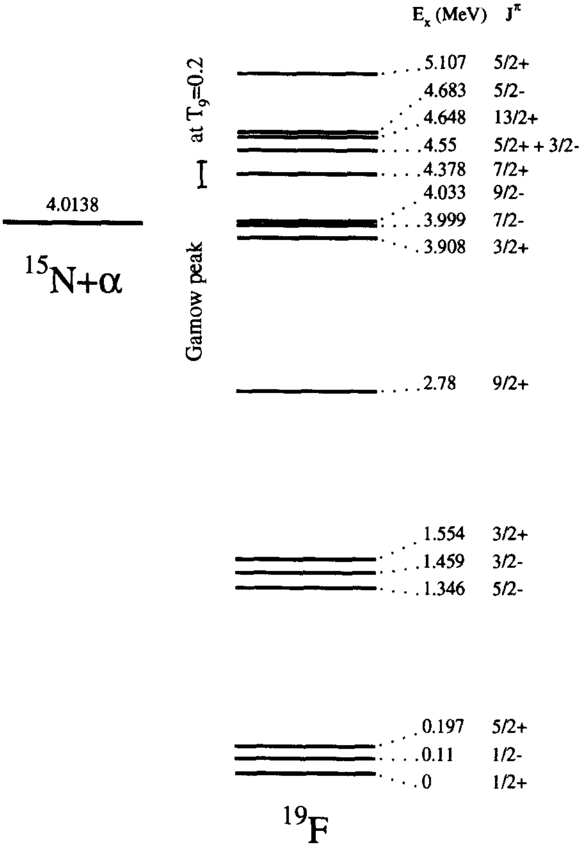

Fig. 2. $^{19}$F energy level diagram. The 16 first levels were studied in this work. The domain of astrophysical interest (typically $T_9 \simeq 0.2$, equivalent to $E_{\mathrm{Gamow}} \simeq 360$ keV) is just in the region of the 4.378 MeV level as shown by the Gamow peak represented as a vertical segment.

$\phi$ = 5 mm) nickel windows and was collected in a Faraday cup positioned behind. Energy loss in the entrance window and gas reduced the beam energy to 27.3 MeV. The ion currents on the Faraday cup and on the target were continuously monitored during the experiment. The particles produced in the target were allowed to exit through a mylar window (65 × 10 mm$^2$ and 3.5 μm thick). The reaction products were analysed by a split pole magnetic spectrometer and detected in the focal plane by a position- and angle-sensitive, 128 wire drift chamber. Clear identification of the particles was allowed by the measurement of energy loss in a proportional counter, and remaining energy with a plastic scintillator. A nozzle fixed to the entrance slits of the spectrometer and aimed at the cell center was used to define the interaction zone and, together with a suitable cell shape, ensures that particles emitted from the nickel windows of the gas cell could not enter the spectrometer (see Fig. 3).

The intensity of the $^7$Li beam was kept around 30 nA. A Si-detector, 100 μm thick, situated within the reaction chamber was used for monitoring through the intensity of

3.5um Mylar = 3.5um*1.39e6 ug/cm3 = 3.5*139ug/cm2=487ug/cm2
0.6um Nickel = 0.6um*7.81e6 ug/cm3 = 0.6*781ug/cm2=467ug/cm2

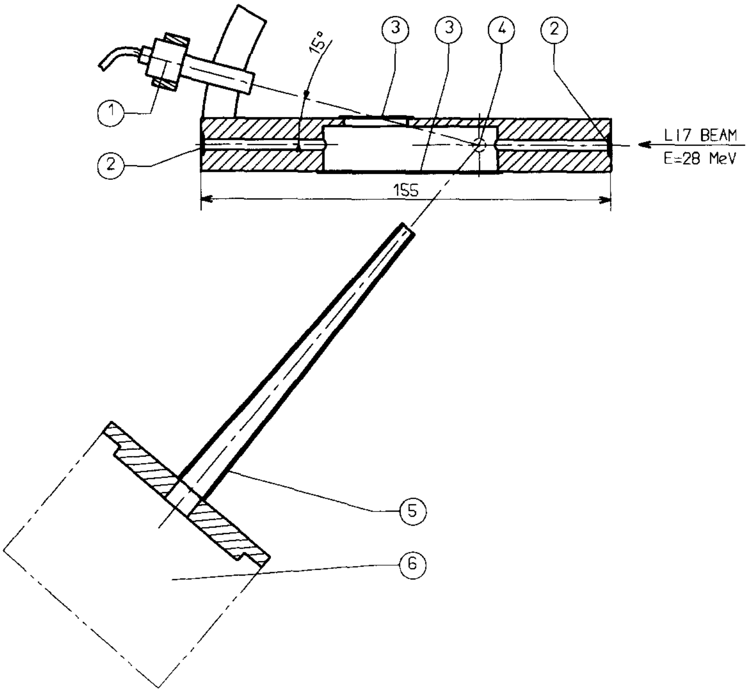

Fig. 3. Confined gas target assembly. (1) Si detector (monitor), (2) nickel window, (3) mylar window, (4) optical center, (5) nozzle and (6) magnetic spectrometer entrance.

the elastically scattered $^7$Li particles. It was located at 15° with respect to beam direction and was shielded by an aluminium foil against electrons.

A Monte Carlo simulation was used to determine the quantity $\Delta\Omega \times \Delta x$, i.e. the geometric solid angle times the effective target thickness seen by the detection system as a function of the observation angle. It was found to range from $10^{-2}$ to $10^{-3}$ sr·cm when $\theta$ varies from 10° to 60° in the laboratory system. (The effective thickness as seen by the spectrometer depends on the observation angle and slit apertures but is of the order of 2 cm, i.e. 0.3 mg/cm$^2$ at 100 mbar). Energy straggling in the thin nickel foil of the entrance window, in the mylar window for the outgoing particles and in the gas limited the resolution to $\approx$ 100 keV (FWHM), depending on the target pressure and scattering angle. That was good enough to allow a clear separation of the peak of interest (Fig. 4). The energy calibration for the experimental spectra was based on known levels of $^{19}$F. Corrections were applied for energy losses in the exit window ($\Delta E \approx$ 160 keV, depending on angle) and in the gas ($\Delta E \approx$ 450 keV at a pressure of 100 mbar). A small gas leakage ($\approx$ 10 mbar per hour) was compensated by a periodic inflow of gas. Spectrograph aberrations due to the finite thickness of the gas target were software corrected using the angular information from the multiwire drift chamber. Angular distributions were obtained from 10° to 60° in the lab system (approximately 12° to 80° in the center of mass system). Owing to the very clean spectra obtained, where all peaks correspond to $^{19}$F levels (Fig. 4), the energy calibration, from the

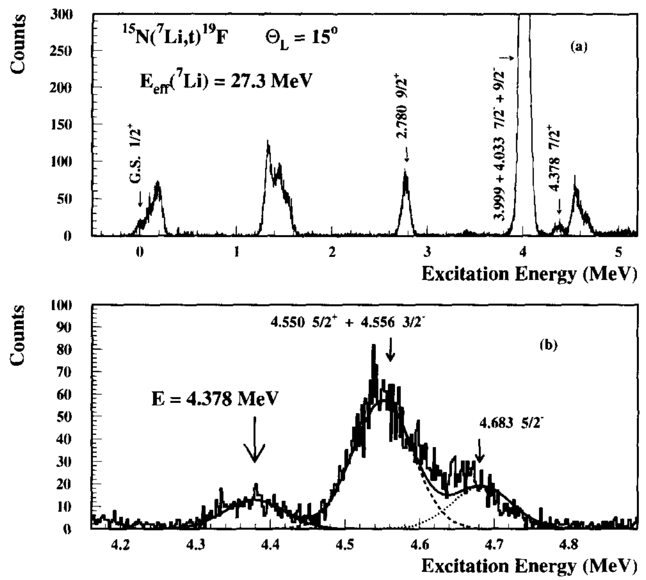

Fig. 4. (a) Typical forward angle triton energy spectrum (all these peaks are $^{19}F$ levels). (b) The level of interest, at $E_x$ = 4.378 MeV, has a resolution close to 100 keV (FWHM) which is enough for an easy deconvolution. Peaks are labeled with spin and parity taken from [16].

ground state up to 5 MeV of excitation energy, was straightforward.

The triton spectrum is shown in Fig. 4a. Only the state at 2.780 MeV is clearly isolated in the $^{19}F$ spectrum. The level of main interest at $E_x$ = 4.378 MeV is weakly populated but can be easily resolved from the group of levels at 4.55 MeV at all angles (Fig. 4b). The triplets of states at 0., 0.110, 0.197 MeV and 1.346, 1.459, 1.554 MeV respectively can be unfolded since the energy separation between the peaks is of the order of the energy resolution. For the intensity of the peaks, the error induced by the deconvolution procedure is estimated to be less than 20% from considerations of spectra obtained at 20° with the solid target where the peaks are well separated owing to the better energy resolution. No attempt was made to extract the individual contributions of the states at 3.908, 3.999 and 4.033 MeV in view of their too small energy separation and of the weakness of the $E_x$ = 3.908 MeV contribution. Only the sum of their contributions is considered here. In the group of peaks corresponding to an excitation energy of about 4.6 MeV (see Fig. 4b) the states at 4.550 and 4.556 MeV are considered as a single level as well as the doublet of levels at 4.648 and 4.683 MeV. It was checked that using a two-level or a three-level deconvolution procedure for this group does not influence the extracted intensity of the level at 4.378 MeV. In spite of its very weak intensity, it was possible to analyse the peak corresponding to the level at 5.107 MeV as it is well separated from neighbouring levels.

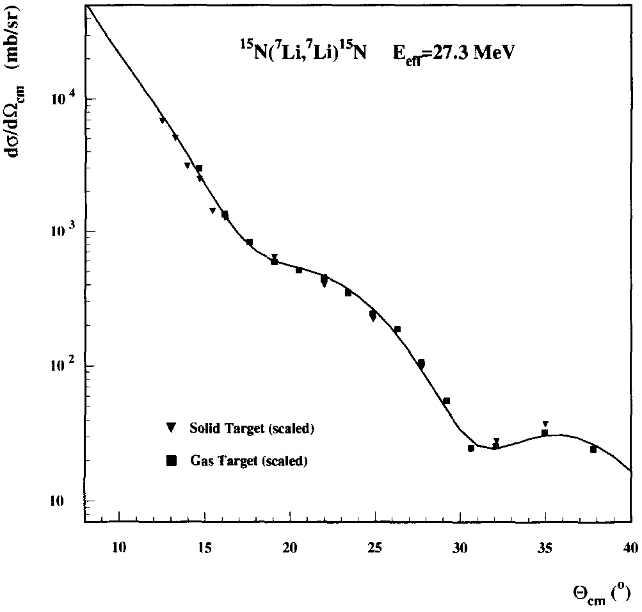

Fig. 5. Elastic scattering cross sections (this work) measured with the $^{15}N$ gas target (squares) and $^{15}N$ enriched melamine solid target (triangles) are compared with the results (solid line) of Woods et al. [17] derived from their absolute experiment. The same global normalization factor has been applied to the data points (see text).

### 2.2. Absolute normalization

The elastic scattering of $^7Li$ on $^{15}N$ was measured from 10° to 60° (lab.) using the same experimental set-up. Our experimental data are shown in Fig. 5, together with the result given by the optical potential parameters from Woods et al. [17] (solid line). They were extracted from an experiment using a solid target and at approximately the same energy (28.8 MeV) as ours and they reproduce very well their data. The shapes of the angular distributions are found to be in remarkable agreement, proving the validity of our procedure concerning the Monte Carlo determination of the evolution of the effective target thickness and solid angle with emission angle.

In order to obtain an absolute value for the cross sections, we performed a normalization experiment with solid targets of melamine $C_3H_6N_6$ ($\approx 100\,\mu g/cm^2$), enriched to 99% in $^{15}N$. We were able to measure the elastic scattering cross section at various angles and the transfer reaction $^{15}N(^7Li,t)^{19}F$ cross section at 20° in the lab system where the contaminant peaks do not obliterate the interesting peaks. The melamine targets were deposited onto foils of 30 $\mu g/cm^2$ of carbon. A gold layer (30 $\mu g/cm^2$) was also deposited over the melamine to prevent rapid evaporation at beam impact. The $^{15}N$ content times beam intensity was monitored by a 1000 $\mu m$ Si detector positioned at $\theta = 25°$. The absolute value of the product beam current times $^{15}N$ content was obtained from normalization of the elastic scattering data to the results given by Woods et al. [17] (15% estimated uncertainty). This normalization factor was then applied to the elastic scattering and transfer reaction data obtained with the gas target. Using this procedure, the results obtained in the transfer reaction for the strongly populated levels at 4.0 MeV agree well (10%) for solid and gas targets at the angle (20°) where the transfer reaction could be measured with both targets.

## 3. Data analysis and discussion

### 3.1. DWBA

Many studies [18,19,14,24] have shown the interest of the approximation of the $\alpha$-cluster model for the stripping reaction ($^7$Li,t). So here we reduce the four-nucleon transfer to a three-body problem ($^{15}$N, $\alpha$, t) where both projectile and residual nuclei have a cluster structure ($^7$Li= $\alpha$ + t, $^{19}$F= $\alpha$ + $^{15}$N). This mechanism of direct transfer is in competition with the compound-nucleus one (see Section 3.5). The analysis was done with the PTOLEMY code [21], but we also used the DWUCK 5 code [22] to check the consistency of the results. The calculations were done with the standard approximation of the interaction $V_{\mathrm{eff}}$ in the post form. The transferred orbital momentum ($L_t$) is one of the parameters of the calculation. In order to calculate the wave functions in the $\alpha$-cluster model, assuming a 0s motion for the four nucleons in the $\alpha$ ($n = l = 0$), we used the usual relationship: the number $N$ of radial nodes (origin excluded) of the $\alpha$ wave function for an orbital angular momentum $L$ is fixed by the relation [23] $2N + L = Q = \sum_{i=1}^{4} (2n_i + l_i)$ deduced from the harmonic oscillator shell model using the rule that the total number of oscillator quanta $Q$ is conserved.

Here $n_i$, $l_i$ are the quantum numbers of the transferred particles in the shell-model levels which contribute to the cluster. It is uniquely defined once the distribution of the individual nucleons of the cluster in the orbitals of the shell model is specified. The program calculates the cross sections for all possible values of transferred orbital momentum using the full distorted-wave Born approximation and adds the resulting cross sections together with the appropriate coefficients.

Finally, calculations of the DWBA transfer cross sections involve the combination of four elements:

(i) the bound-state wave function representing the composite projectile nucleus $^7$Li= $\alpha$ + t and the associated potential $V_{\alpha t}$,

(ii) the bound-state wave function representing the composite nucleus $^{19}$F= $\alpha$ + $^{15}$N in the final state,

(iii) the elastic scattering wave function in the incoming channel $^{15}$N($^7$Li, $^7$Li)$^{15}$N and

(iv) the elastic scattering wave function in the outgoing channel $^{19}$F(t,t)$^{19}$F.

These elements are discussed in detail below.

### 3.2. Wave function of $^7Li=\alpha+t$ and effective interaction

The $\alpha$-cluster structure in the $^7$Li nucleus has been studied extensively. We used interaction potentials with the usual Woods–Saxon shape while the Coulomb potential is of a uniform charge distribution. Kubo and Hirata [24] have determined a parameter set for the effective interaction $V_{\alpha t}$ between the $\alpha$-cluster and the tritium core from $^3$He–$^4$He scattering (see Table 1). Other parameter sets [25,26] were used in this work to check the sensitivity of the results to the effective interaction. The depth of each potential is adjusted by calculating the wave function so that the known experimental separation energy for the $\alpha$ cluster, 2.47 MeV, can be reproduced.

The $\alpha$-cluster has been considered to be in a relative p-wave state inside $^7$Li so that $N = 1$ and $L = 1$. Another parameter is the $\alpha$ spectroscopic factor in $^7$Li. It is directly related to the $\Gamma_\alpha$ we want to determine. Several values are reported from different studies: 0.95 [19], 1.0 [18], and 1.2 (shell-model value [20]). The average is close to unity and we adopted the value of $S_\alpha(^7\text{Li}) = 1$, keeping in mind that the final results suffer from the uncertainty in this parameter.

### 3.3. Wave functions of the transferred $\alpha$-cluster

In the context of the simple cluster model, the states of $^{19}$F nucleus are interpreted in terms of a single-particle $\alpha$ cluster and an inert $^{15}$N core and are characterized by $N$ and $L$ quantum numbers. To each of these states the $\alpha$ spectroscopic factor $S_\alpha(^{19}\text{F}) = |\langle ^{19}\text{F}|^{15}\text{N}+\alpha\rangle|^2$ is associated.

The $^{19}$F states at $E_x = 0.110$ MeV ($J^\pi = 1/2^-$), 1.346 ($5/2^-$), 1.459 ($3/2^-$), 3.999 ($7/2^-$), 4.033 ($9/2^-$) can be described as a $p_{1/2}$ proton hole weakly coupled to the $0^+$, $2^+$ and $4^+$ states of $^{20}$Ne. They have been identified with members of the $^{15}$N+$\alpha$ cluster configuration with $Q = 2N + L = 8$ [27,14] and their $\alpha$-spectroscopic factors are known to be large; we too adopted this configuration for all negative parity states.

For the other levels with positive parity the choice of cluster representations is not unambiguous and we made the calculations with both $2N + L = 7$ and 9, even though we expect that for such low excitation energy they should be populated mainly by the $2N + L = 7$ cluster transfer [28].

We used the $\alpha$-core potential for fluorine from Kubo and Hirata [24]. It has a Woods–Saxon shape with $a_r = 0.7$ fm, $r_r = 1.3$ fm, and the well depth is adjusted to reproduce the experimental separation energy of the $\alpha$. For unbound levels, as usual, we impose a binding energy of 0.05 MeV.

### 3.4. Distorting potentials

In $\alpha$-transfer DWBA calculations, the final result is very dependent on the optical-model parameters for the elastic scattering of the incoming particle. As mentioned in Section 2.2, this reaction $^{15}$N($^7$Li, $^7$Li)$^{15}$N has already been measured by Woods et al. [17] at 28.8 MeV. Our own experiment was run at an effective beam energy

Table 1
Optical potential parameter sets

| Potential | $V$ (MeV) | $r_r$ [a] (fm) | $a_r$ (fm) | $W$ (MeV) | $r_i$ [a] (fm) | $a_i$ (fm) | $r_c$ [a] (fm) |
|---|---|---|---|---|---|---|---|
| $\alpha$+t [b] | 93.7 | 1.3 | 0.7 | | | | 1.3 |
| $^{15}$N+$^{7}$Li [c] | 284.7 | 0.84 | 0.907 | 8.982 | 2.416 | 0.670 | 1.3 |
| $^{15}$N+$^{7}$Li [d] | 246. | 0.9 | 0.907 | 7.6 | 2.42 | 0.7 | 1.3 |
| $^{19}$F+t [e] | 104.3 | 1.10 | 0.77 | 30.1 | 1.29 | 1.06 | 1.3 |

[a] The relation $R = rA_T^{1/3}$ gives $R_r$, $R_i$ and $R_c$.
[b] Ref. [24].
[c] Ref. [17].
[d] This work.
[e] Ref. [31].

of 27.3 MeV. In Table 1 the corresponding sets of optical potential parameters are presented. Both give a very good description of the experimental elastic cross section.

For the tritium elastic scattering on fluorine, we used the sets of parameters available at energies close to ours, resulting from analysis of systematics [29] from a measurement at $E = 33$ MeV [31] or from $^3$He elastic scattering at $E = 25$ MeV [32]. We chose the potential of Ward and Hayes [31] as its extraction is the most direct.

### *3.5. Analysis of the data*

The extraction of spectroscopic factors from the transfer reaction is based on the hypothesis that the reaction is direct. At our beam energy this condition may not be absolutely fulfilled, but we can expect that at forward angles the direct part is dominant. At larger angles however, compound nuclear contributions can be large. We calculated the compound nuclear contribution to the cross section in the framework of the Hauser–Feshbach statistical model with a modified version of the program HSFB [33]. Several outgoing channels were taken into account and optical potentials were extracted from Ref. [29]. This HSFB contribution was added incoherently to the DWBA part of the cross section so that the calculated cross section (to be fitted to the experimental one) is given by

$$\left(\frac{d\sigma}{d\Omega}\right) = S\left(\frac{d\sigma}{d\Omega}\right)_{\rm DWBA} + C\left(\frac{d\sigma}{d\Omega}\right)_{\rm HSFB}, \qquad (1)$$

where $C$ is a normalization constant (see Section 3.5) and $S$ is the spectroscopic factor and is related to the lithium and fluorine spectroscopic factor by

$$S = S_\alpha(^7{\rm Li})\, S_\alpha(^{19}{\rm F}) = S_\alpha(^{19}{\rm F}), \qquad (2)$$

since $S_\alpha(^7\mathrm{Li}) = 1$.

Experimental results are presented in Fig. 6–9, together with the results of our calculations. They show that the cross sections fall rapidly, down to 10 μb/sr, with increasing angles as expected from a direct process. The angular distributions are rather structureless, due to the fact that several values of the transferred angular momenta $L_t$ are mixed in the cross section. These different contributions are presented in Fig. 8 (top) for the 2.780 MeV level. Maxima and minima from different $L_t$ values build up together to give a smooth curve peaked at small angles. The solid lines are the sum of the direct part (point-dashed lines) and the HSFB contribution (dotted lines). The values of the spectroscopic factor $S$, defined by the relation (1), are shown in the figures. The calculated HSFB contribution has been renormalized by a factor $C = 0.3$ (see Eq. (1)) in order to obtain a compound-nucleus cross section similar to the data at large angles for the weakly populated level at $E_x = 5.107$ MeV (see Fig. 7) as it displays one of the less forward peaked structure. The same factor was then successfully applied to the HSFB contributions of the other levels. The very good overall agreement with the data shows that the reaction proceeds through a direct $\alpha$-cluster transfer mechanism added to a small part of compound-nucleus contribution (for the level of astrophysical interest, see Fig. 9).

### 3.6. *Stability of the results*

#### 3.6.1. *Stability of the spectroscopic factors*

We carefully studied the stability of the results with respect to the various parameters entering into the calculations [15]. No significant difference was found between the results obtained with the codes PTOLEMY and DWUCK 5. Only slight shape alterations were found when using the different incoming distorting potentials from Table 1. A small difference in the shape is observed when changing significantly the outgoing distorting potential. However, the normalization, and hence the spectroscopic factors, are little affected ($\approx$10%) since the differences affect mostly the largest angles. The same is true when using the 'prior' instead of the 'post' scheme in DWBA analysis ($\approx$ 20% difference).

Uncertainties arise from the choice of the $^7$Li = $\alpha$ + t potential. Calculations for these different potentials are compared in Fig. 8b for the $E_x = 1.346$ MeV level. Potentials from Refs. [25,26] gave smaller values for the spectroscopic factors: for the 4.378 MeV level the fluorine spectroscopic factor $S_\alpha$ ($^{19}$F) was found smaller by a factor 0.6 (with the same value of $S_\alpha(^7\text{Li}) = 1.$). These two are very general potentials and are not particularly adapted to this nucleus. The Kubo and Hirata [24] potential was used in this work since it gives the best overall shape fitting to the data. Table 1 displays the sets of potential parameters chosen for this work.

The influence of the $\alpha$-core potential in fluorine was found to be important for the spectroscopic factors. For instance, when a variation of ±0.1 fm for $a_r$ and ±0.5 fm for $R_r$ are applied to the $\alpha$-$^{15}$N potential, the spectroscopic factors show important variations (up to a factor of 2).

#### 3.6.2. *Stability of the $\alpha$ reduced width*

The $\alpha$-reduced width is given [30] by the relation

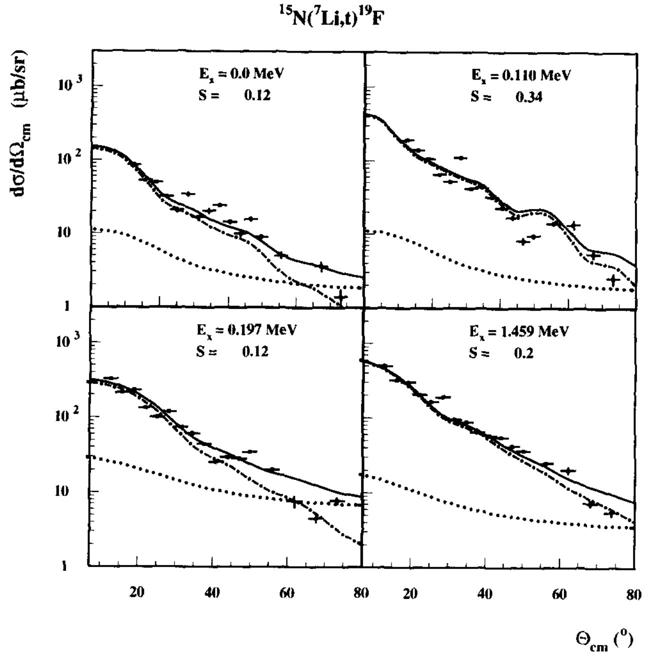

Fig. 6. Differential cross sections for the reaction $^{15}$N($^7$Li,t)$^{19}$F on the $E_x$ = g.s., 0.110, 0.197 and 1.459 MeV levels. The solid line is the sum of the DWBA contribution (dot-dashed curves) and of the compound-nucleus part (dotted lines). Only statistical errors are displayed.

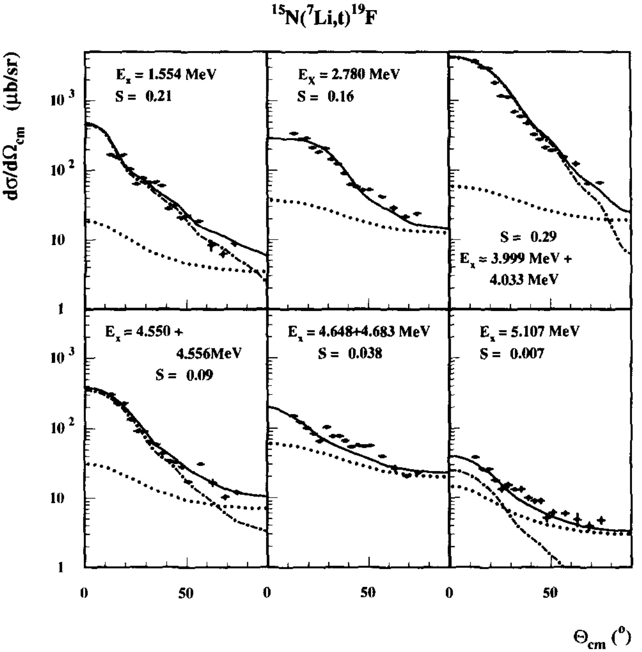

Fig. 7. Same as Fig. 6 for the levels at $E_x$ = 1.554, 2.780, 3.999+4.033, 4.550+4.556, 4.648+4.683 and 5.107 MeV. The direct reaction part of the cross section corresponding to the 4.550+4.556 MeV and 4.648+4.683 MeV peaks have been assumed to be predominantly due to the $E_x$ = 4.550 and 4.683 MeV levels respectively.

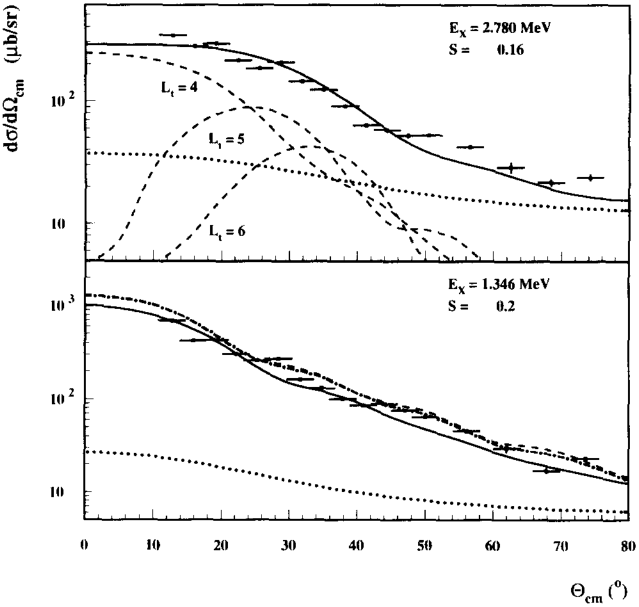

Fig. 8. (a) (top) Contributions for the different transferred orbital angular momenta ($L_t$) are presented in the case of the 2.780 MeV level together with their sum. (b) (bottom) DWBA differential cross sections obtained with the same spectroscopic factor ($S = 0.2$) but with different sets of parameters for the $\alpha$+t potential: [24] (solid line), [25] (dashed line) and [26] (dot-dashed line). In each case the dotted curve represents the compound-nucleus contribution.

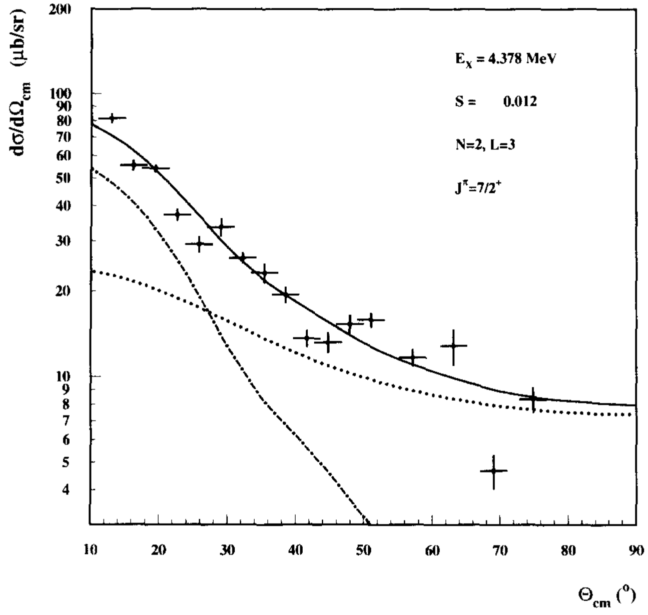

Fig. 9. Differential cross section for the level of astrophysical interest at $E_x$ = 4.378 MeV. The solid line is the sum of the DWBA contribution (dot-dashed curves) and of the compound-nucleus part (dotted lines). At forward angle, the direct contribution dominates the transfer reaction.

$$\gamma_\alpha^2 = \frac{\hbar^2 r}{2\mu_\alpha}|\mathcal{R}_L(R_I)|^2 , \tag{3}$$

where $R_I$ is the interaction radius, $\mu_\alpha$ is the reduced mass of the $^{15}$N + $\alpha$ system, $\mathcal{R}_L$ is the radial part of the $\alpha$-cluster wave function $\left(\int_0^\infty \mathcal{R}_L^2 r^2 dr = 1\right)$ which is related to the model wave function used in the distorted-wave calculations by

$$\mathcal{R}_L(R_I) = \sqrt{S_\alpha}\,\mathcal{R}_L^{\mathrm{DW}}(R_I) . \tag{4}$$

At a given value of $R_I$, the final results are not as sensitive as the spectroscopic factors to the $\alpha$-core potential. For example, the effect of a factor of two change in the spectroscopic factor of the 0.110 MeV level, result only in a change of 15% in the $\alpha$-reduced width. In return, the reduced width $\gamma_\alpha^2$ was found to be highly sensitive to the interaction radius $R_I$ but due to the penetration factor, the $\alpha$-width $\Gamma_\alpha$ is much less sensitive (a factor of two between $R_I = 5$ and $R_I = 6$ fm however). We finally adopted $R_I = 5$ fm.

Further uncertainties come from the configuration for positive parity levels. Since the choice is not unambiguous, in the following, we present both the results for the $2N + L = 7$ and 9 configuration but we will adopt as final result the value corresponding to the lowest configuration.

From the above discussion of the uncertainties in the parameters, we estimate that the corresponding overall error on the $\alpha$-widths is of a factor of 2. This estimated error is further supported by the comparison between the present results and the $\alpha$-widths obtained by direct measurements (see Table 3).

### 3.7. Results

In a first step fluorine spectroscopic factors $S_\alpha$ are extracted from experimental data using Eq. (1) and the corresponding values are presented in Table 2 for the various $2N + L$ configurations. In a second step, the reduced $\alpha$-widths $\gamma_\alpha^2$ are calculated with Eq. (3) at $R_I = 5$ fm. For comparison with other studies, we introduce the associated dimensionless $\alpha$-reduced width $\theta_\alpha^2$:

$$\theta_\alpha^2 = \frac{\gamma_\alpha^2(R_I)}{\gamma_{\mathrm{W}}^2(R_I)} , \tag{5}$$

where $\gamma_{\mathrm{W}}^2(R_I)$, the Wigner limit, is equal to 0.793 MeV. For unbound levels, the $\alpha$-width $\Gamma_\alpha$ can be calculated [30] by

$$\Gamma_\alpha = 2\gamma_\alpha^2(R_I) P_L(Q_\alpha, R_I) , \tag{6}$$

where the effect of the Coulomb barrier is taken into account by using the $\alpha$-penetrability factor $P_L(Q_\alpha, R_I)$ for an $\alpha$-decay energy $Q_\alpha$. All these factors are presented in Table 2. In Table 2, we observe that the low-lying negative parity states in $^{19}$F have high spectroscopic factors. They are described as arising from the coupling of a $p_{1/2}$ hole to the

Table 2
Results

| $E_x$ (*MeV*) | $J^\pi$ | $2N+L$ | $S_\alpha$ $\times10^{-2}$ | $\theta_\alpha^2$ [a] $\times10^{-2}$ | $\gamma_\alpha^2$ (keV) | $\Gamma_\alpha$ (eV) |
|---|---|---|---|---|---|---|
| g.s. | $\frac{1}{2}^+$ | 7 | 12. | 5.3 | 42. | |
| | | 9 | 8. | 5.0 | 40. | |
| 0.110 | $\frac{1}{2}^-$ | 8 | 34. | 18.7 | 148. | |
| 0.197 | $\frac{5}{2}^+$ | 7 | 12. | 3.9 | 31. | |
| | | 9 | 7. | 3.7 | 29. | |
| 1.346 | $\frac{5}{2}^-$ | 8 | 20. | 10.6 | 84. | |
| 1.459 | $\frac{3}{2}^-$ | 8 | 20. | 10.8 | 86. | |
| 1.554 | $\frac{3}{2}^+$ | 7 | 21. | 10.4 | 82. | |
| | | 9 | 14. | 9.1 | 72. | |
| 2.780 | $\frac{9}{2}^+$ | 7 | 16. | 3.2 | 25.4 | |
| | | 9 | 7.5 | 3.1 | 24.6 | |
| 3.908 | $\frac{3}{2}^+$ | 7 | $\leqslant 9.$ | $\leqslant 5.$ | $\leqslant 40$ | |
| | | 9 | $\leqslant 7.$ | $\leqslant 4.5$ | $\leqslant 36$ | |
| 3.999 [b] | $\frac{7}{2}^-$ | 8 | 29. | 13.5 | 109. | |
| 4.033 [b] | $\frac{9}{2}^-$ | 8 | 29. | 13.5 | 109. | |
| 4.378 | $\frac{7}{2}^+$ | 7 | 1.2 | 0.56 | 4.44 | $1.5\times10^{-9}$ |
| | | 9 | 0.75 | 0.47 | 3.73 | $1.25\times10^{-9}$ |
| 4.550 [c] | $\frac{5}{2}^+$ | 7 | 9. | 4.2 | 33. | $1.6\times10^{-5}$ |
| | | 9 | 5.5 | 3.5 | 27.5 | $1.3\times10^{-5}$ |
| 4.683 [d] | $\frac{5}{2}^-$ | 8 | 3.8 | 2.4 | 18.7 | $3.0\times10^{-3}$ |
| 5.107 | $\frac{5}{2}^+$ | 7 | 0.7 | 0.33 | 2.6 | $3.3\times10^{-2}$ |
| | | 9 | 0.4 | 0.25 | 1.98 | $2.5\times10^{-2}$ |

[a] Calculated with $R_l = 5$ fm.

[b] Assuming the same internal structure and hence the same $S_\alpha$ for the levels at 3.999 and 4.033 MeV.

[c] Neglecting the contribution of $E_x = 4.556$ MeV, $J^\pi = \frac{3}{2}^-$ level.

[d] Neglecting the contribution of $E_x = 4.648$ MeV, $J^\pi = \frac{13}{2}^+$ level.

four-particle states of the ground-state rotational band in $^{20}$Ne. Hence a strong excitation of these levels in the ($^7$Li,t) reaction is expected and was indeed clearly observed in Ref. [13]. Identifying these states with members of the $^{15}$N + $\alpha$ cluster band with $2N+L = 8$, Kubo et al. [14], using the Middleton experiment data [13], have extracted a mean spectroscopic factor value of 0.24 for these levels. For positive parity levels, differences between the $2N+L = 7$ and 9 configurations seem large (a factor of 1.5) when comparing spectroscopic factors. However, when the physical parameters $\gamma_\alpha^2$ are calculated, the discrepancy is reduced to less than 25%. This will come out as an additional source of uncertainty on the astrophysical rate but of acceptable magnitude. For the rest of the study we will use the $2N + L = 7$ results. For unbound levels, some $\alpha$-widths were already measured. It is especially interesting to compare direct measurements with our results (see Table 3), as it provides a test for the indirect method of extracting $\alpha$-widths. The $\alpha$-width of the 4.683 MeV level is known to be $(2.1\pm0.7)\times10^{-3}$ eV [34] which is in good agreement with our value of $3.0\times10^{-3}$ eV. Magnus [35] gave $\Gamma_\alpha = (3.2 \pm 0.7)\times10^{-5}$ eV and $\Gamma_\alpha < 5 \times 10^{-6}$ eV for the levels at $E_x = 4.550$ MeV

Table 3
Comparison between direct and indirect measurements

| $E_x$ (MeV) | $J^\pi$ | $\Gamma_\alpha$ (eV) | |
|---|---|---|---|
| | | direct | This work |
| 4.550 | $\frac{5}{2}^+$ | $(3.2\pm0.7)\times10^{-5}$ [a] | $1.6\times10^{-5}$ [d] |
| 4.556 | $\frac{3}{2}^-$ | $< 5\times10^{-6}$ [a] | |
| 4.683 | $\frac{5}{2}^-$ | $(2.1\pm0.7)\times10^{-3}$ [b] | $3.0\times10^{-3}$ [e] |
| 5.107 | $\frac{5}{2}^+$ | $> 2.\times10^{-2}$ [c] | $3.3\times10^{-2}$ |

[a] Ref. [35].
[b] Ref. [34].
[c] Ref. [36].
[d] Neglecting the contribution of $E_x$ = 4.556 MeV level.
[e] Neglecting the contribution of $E_x$ = 4.648 MeV level.

and 4.556 MeV respectively. Neglecting the direct contribution of the 4.556 MeV in our measurement as indicated by the results of Ref. [35], we obtain $\Gamma_\alpha = 1.6\times10^{-5}$ eV for the level at 4.550 MeV in reasonable agreement with the direct measurement of Magnus. For the 5.107 MeV level, a limit $\Gamma_\alpha > 2.\times10^{-2}$ eV is extracted from [36,37] in agreement with our value of $3.3\times10^{-2}$ eV. The $\alpha$-width of the level of astrophysical interest has been determined to be $\Gamma_\alpha = (1.5^{+1.5}_{-0.8})\times10^{-9}$ eV. The error (a factor of two) has been estimated from the analysis of the stability of results and from the comparison between direct and indirect measurements presented above.

## 4. The new $^{15}$N($\alpha,\gamma$)$^{19}$F reaction rate

For astrophysical calculations, we provide the expression for the reaction rate in the formulation of Fowler et al. For a narrow and isolated resonance the reaction rate could be written as [38]

$$N_A\langle\sigma v\rangle = C_8 T_9^{-\frac{3}{2}} \exp\left(-\frac{C_9}{T_9}\right) \tag{7}$$

with $C_8 = 1.53986\times10^5\mu^{-3/2}\omega\gamma$, $C_9 = 11.605\ E_R$, where $\omega\gamma$ is the strength of the resonance in eV, $\mu$ the reduced mass in atomic mass units, $E_R$ the resonance energy in MeV, $T_9$ the temperature in billions of degrees and $N_A\langle\sigma v\rangle$ is expressed in cm$^3$s$^{-1}$mole$^{-1}$.

The strength is given by

$$\omega\gamma = \frac{2J_R+1}{(2J_T+1)(2J_p+1)}\frac{\Gamma_\alpha\Gamma_\gamma}{\Gamma_T}, \tag{8}$$

where $J_R$, $J_T$ and $J_p$ are the intrinsic angular momenta of the resonance level, target and projectile respectively and $\Gamma_\alpha$, $\Gamma_\gamma$ and $\Gamma_T$ are the $\alpha$, $\gamma$ and total width respectively. The last term can be simplified in this case since $\Gamma_T \approx \Gamma_\alpha \ll \Gamma_\gamma$, so that $\Gamma_\gamma\Gamma_\alpha/\Gamma_T = \Gamma_\alpha$.

Table 4
Isolated resonance parameters

| $E_x$ (MeV) | $E_r$ (MeV) | $\omega\gamma$ (eV) | $C_8$ |
|---|---|---|---|
| 4.378 | 0.364 | $(6.^{+6.}_{-3.})\times10^{-9}$ [a] | $1.645\times10^{-4}$ |
| 4.550 | 0.536 | $(9.7\pm2.0)\times10^{-5}$ [b] | 2.66 |
| 4.683 | 0.669 | $(6.0\pm1.)\times10^{-3}$ [c] | $1.645\times10^{2}$ |

[a] This work.
[b] Ref. [35].
[c] Ref. [34].

From the new value of $\Gamma_\alpha$ for the 4.378 MeV level, we deduced $\omega\gamma = (6.^{+6.}_{-3.})\times10^{-9}$ eV. Two other levels have been considered, for the calculation of the reaction rate: the 4.550 MeV and 4.683 MeV levels for which we used the $\omega\gamma$ values from Ref. [35] and [34] that are displayed in Table 4. With $l = 7$, the $E_x = 4.648$ MeV level is strongly inhibited and has never been seen in $^{15}\mathrm{N}(\alpha,\gamma)^{19}\mathrm{F}$. The continuum term for the highest temperatures has also been modified relative to CF88. This is the result of the fit of the sum of the contributions from the ≈ 60 resonances from 5 MeV to 10 MeV whose strengths are tabulated in [16].

In CF88, the low temperature continuum only represents the tail of the broad $E_x$ = 5.50 MeV level. In addition, we calculated the contributions of direct capture for the six first $^{19}$F levels as with the RACAP code [39] and of the sub-threshold ($l = 1$) $E_x$ = 3.908 MeV level. (The contributions of the ($l = 4$) near-threshold levels $E_x$ = 3.999 and 4.033 MeV are negligible.) The total contributes significantly to the rate only below $T_9 = 0.07$, i.e. for vanishing values of the reaction rate.

Finally, the new reaction rate is

$$\begin{aligned} N_A\langle\sigma v\rangle = {} & 1.0\times10^{11}\,T_9^{-2/3}\exp\left(-36.215\,T_9^{-1/3}-(T_9/0.6)^2\right) \\ & +1.645\times10^{-4}T_9^{-3/2}\exp(-4.223/T_9)\times(0.5\text{–}2.) \\ & +2.66T_9^{-3/2}\exp(-6.220/T_9) \\ & +1.645\times10^{2}T_9^{-3/2}\exp(-7.764/T_9) \\ & +3.92\times10^{4}T_9^{-1/3}\exp(-14.522/T_9)\,. \end{aligned} \tag{9}$$

The ratio of the new reaction rate to the CF88 one is presented in Fig. 10. The modification brought by our measurement is very important for temperatures lower than $T_9 = 0.2$, since the reaction rate is found lower by a factor of about 60. For $0.4 < T_9 < 0.8$, the reaction rate is higher by a factor of ≈ 10. This effect is due to the contribution of the levels at 4.55 MeV and 4.683 MeV, neglected in CF88.

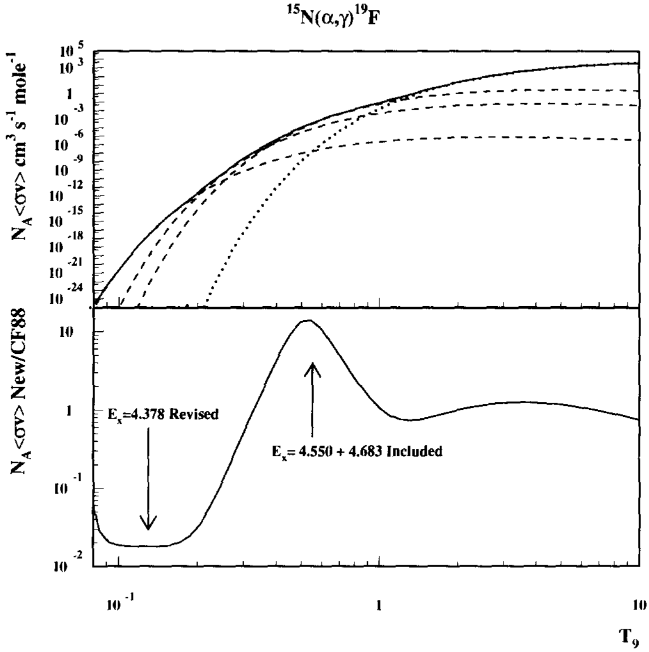

Fig. 10. The new rate. The upper panel displays the new rate (solid line) together with the contributions of the isolated resonances (dashed lines) and high temperature continuum (dotted line). The lower panel shows the ratio of the new rate to the CF88 one. The important decrease in the rate below $T_9 = 0.3$ is due to the reduced $E_x = 4.378$ MeV strength while the increase around $T_9 = 0.5$ is due to the effect of the levels at $E_x = 4.550$ and 4.683 MeV.

## 5. Effect of the $^{15}$N($\alpha,\gamma$)$^{19}$F rate on the synthesis of $^{19}$F in thermal pulses

As indicated in Section 1, $^{15}$N($\alpha,\gamma$)$^{19}$F plays an important role in the $^{19}$F production during thermal pulses in AGB stars [9]. This section illustrates the impact of the $^{15}$N($\alpha,\gamma$)$^{19}$F reaction rate on the $^{19}$F synthesis by comparing the abundances resulting from thermal pulses of a $3M_\odot$ star (with an initial solar composition), when use is made of the CF88 or of the new rate given in Section 4 (referred to as ORSAY in the following). Details concerning the stellar evolution code can be found in Ref. [41]. Complete evolutionary sequences incorporating the new $^{15}$N($\alpha,\gamma$)$^{19}$F ORSAY rate and a detailed discussion of the results are presented elsewhere [40].

The AGB stars are made of a carbon–oxygen core, helium- and hydrogen-burning shells separated by an intershell He zone, and a convective envelope extending up to the surface. Their evolution is characterized by a sequence of thermal runaways (thermal pulses), originating in the He-burning shell and triggering a convective He-burning zone growing rapidly in the intershell region. This is illustrated in Fig. 11 which presents the evolution of two successive thermal pulses of our $3M_\odot$ star. After a pulse, the convective envelope may penetrate the intershell region, thus bringing to the surface the ashes of He-burning from the pulse (third dredge-up, not represented in Fig. 11).

Fluorine is produced in the pulse convective zones by the reaction chain

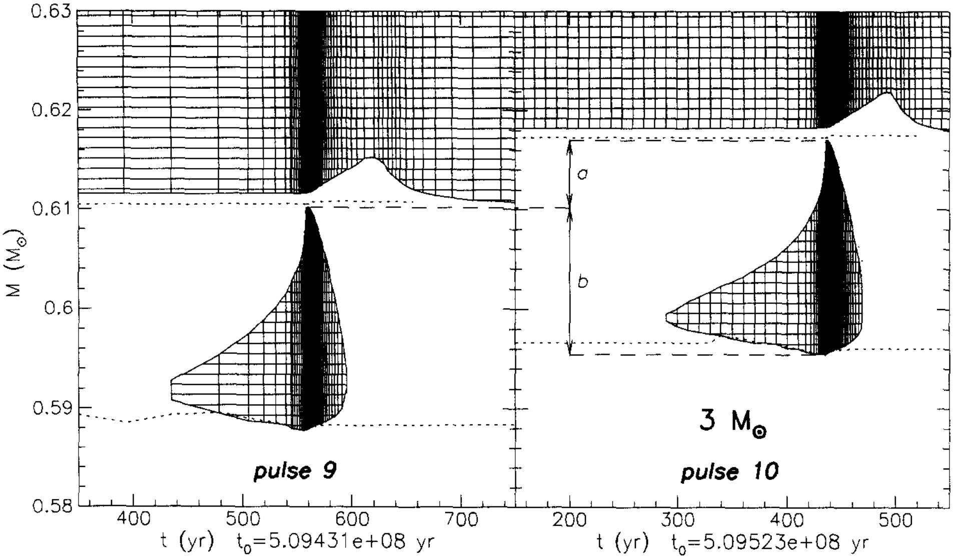

Fig. 11. Structure of the ninth and tenth thermal pulses in a $3M_\odot$ AGB star as a function of time. The ordinate represents the mass (in solar mass units) enclosed in a sphere of given radius within the star (i.e. $M = 0$ at the center and $M = 3M_\odot$ at the surface). The hatched areas correspond to convective regions. Each computed model is represented by a vertical line in the convective zones (horizontal lines have no special meaning). The short-dashed lines indicate the location of maximum energy production by H burning (upper line) or He burning (lower line). Regions *a* and *b* referred to in the text are also indicated.

$^{14}$N$(\alpha,\gamma)^{18}$F$(\beta^+)^{18}$O(p,$\alpha$)$^{15}$N$(\alpha,\gamma)^{19}$F. The necessary protons are produced mainly by $^{14}$N(n,p)$^{14}$C and $^{26}$Al(n,p)$^{26}$Mg, the neutrons coming from $^{13}$C($\alpha$,n)$^{16}$O. The seed nuclei $^{13}$C, $^{14}$N and $^{26}$Al involved in the $^{19}$F production are supplied by the ashes of the former H-burning located in the layers labelled *a* in Fig. 11. These seeds are engulfed in the convective zone during the thermal pulse. With the CF88 rate, $^{15}$N is totally converted into $^{19}$F in the convective region during the thermal pulse. With the lower ORSAY rate, however, the amount of $^{15}$N synthesized in the pulse is only partially converted into $^{19}$F. This is clearly seen in Fig. 12, which displays the $^{19}$F abundance profiles at the time of disappearance of the convective zone associated with the ninth pulse calculated with either the CF88 or the ORSAY rate.

Due to the recurrent nature of the pulses, some fraction of the $^{19}$F produced in a given pulse is incorporated into the next one, depending on the overlap between the two successive pulses (region *b* of Fig. 11). The evolution of the $^{19}$F intershell abundance, i.e. of the $^{19}$F abundance in the region located between the H- and He-burning shells, is thus determined on the one hand by the amount of fluorine produced within the pulses, and on the other hand by the pulse overlaps. This evolution predicted with the ORSAY rate is displayed in Fig. 13b. With the CF88 rate, $^{15}$N is totally converted into $^{19}$F even in the early pulses with low base temperatures (Fig. 13c). As a consequence, the resulting $^{19}$F intershell abundance is larger than the one predicted with the ORSAY rate. However, the difference decreases with increasing pulse number as $^{15}$N is inevitably

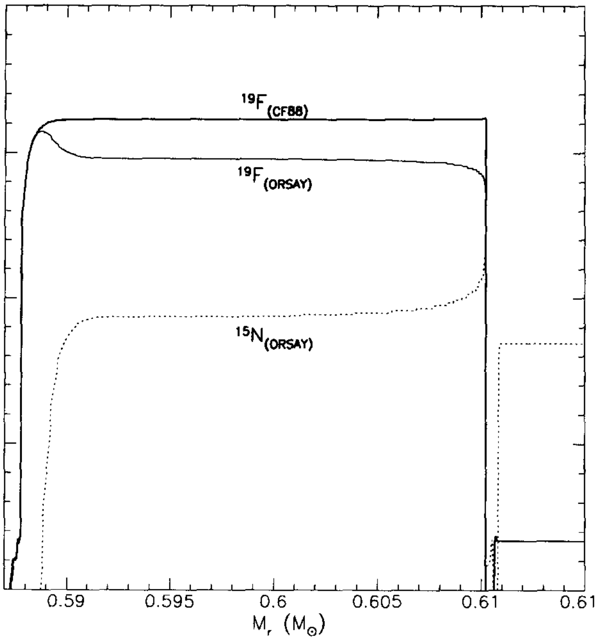

Fig. 12. The $^{15}N$ (dashed line) and $^{19}F$ (solid line) mass fractions as a function of the stellar mass coordinate (see Fig. 11) at the end of the ninth pulse in a $3M_\odot$ AGB star. The thick line corresponds to the $^{19}F$ profile obtained with the CF88 $^{15}N(\alpha,\gamma)^{19}F$ rate, whereas thin lines relate to the ORSAY rate. Note that the $^{15}N$ profile corresponding to the CF88 rate falls below the lower boundary of the figure, as $^{15}N$ is totally converted into $^{19}F$ in the convective region associated with the pulse.

transformed into $^{19}F$ with the ORSAY rate when the pulse temperatures get high enough (Fig. 13c).

The extent to which the ORSAY $^{15}N(\alpha,\gamma)^{19}F$ rate modifies the predictions of the $^{19}F$ surface abundance of AGB stars can be evaluated from Fig. 13a. The $^{19}F$ surface abundance has been estimated by assuming that, after each pulse, the convective envelope of mass $M_e = 2.4M_\odot$ dredges up $\Delta M = 5 \times 10^{-3}M_\odot$ of material from the region previously processed by the thermal pulse (this simplistic assumption is made necessary by the fact that our models, like most of the current ones, are unable to account for the dredge-ups in a self-consistent way). Fig. 13a shows that the surface $^{19}F$ overabundance (with respect to the solar system value) achieved after a given number of pulses is smaller with the ORSAY rate than with the CF88 one. The displayed difference can be considered as a maximum, since it is assumed that the third dredge-up occurs from the first pulse on, when the difference between the ORSAY and CF88 intershell $^{19}F$ abundances is maximum. If the dredge-up were to start occurring at a later pulse, the difference in the $^{19}F$ surface abundances resulting from the ORSAY and CF88 rates would be much smaller.

In conclusion, the new ORSAY $^{15}N(\alpha,\gamma)^{19}F$ rate tends to delay the onset of $^{19}F$ overabundances at the surface of AGB stars. The $^{15}N(\alpha,\gamma)^{19}F$ rate presented in this paper will definitely put the predictions of stellar $^{19}F$ production on firmer grounds, though

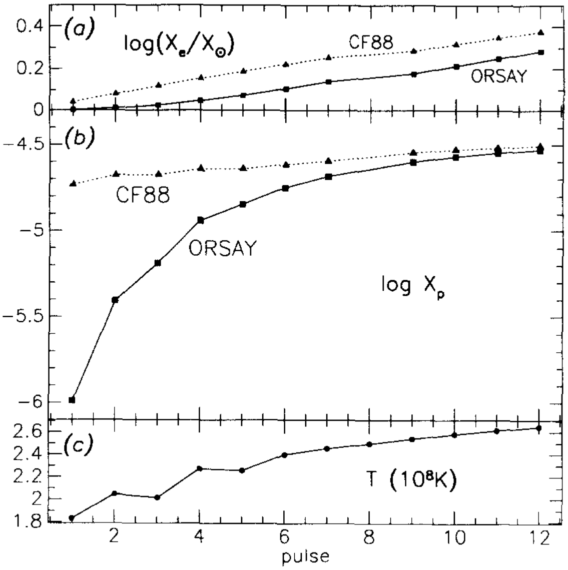

Fig. 13. Evolution of various quantities from the first to the twelfth pulse in the $3M_\odot$ AGB star already considered in Fig. 11. (a) Surface $^{19}$F overabundance with respect to solar if, after each pulse, $5 \times 10^{-3} M_\odot$ of material formerly processed by the thermal pulse is dredged up into the convective envelope (of mass $M_c = 2.4M_\odot$). The filled squares give the surface overabundances predicted with the ORSAY rate, while the filled triangles correspond to the situation encountered with the CF88 rate, where all the available $^{15}$N is converted into $^{19}$F in the pulse (see (b). (b) Mass fractions of $^{19}$F in the intershell zone at the end of each pulse. The filled squares and triangles indicate the predictions obtained with the ORSAY and CF88 rates, respectively. (c) Maximum temperature at the base of the convective shell.

these predictions are still hampered by uncertainties in the modelling of convective processes like the third dredge-up.

## Acknowledgements

Our special thanks go to the Orsay Tandem Accelerator staff for their support during the installation and running of this experiment. We are grateful to M. Mermaz and J. Van de Wiele for their advice at various stages of the analysis. Part of the collaborative work between nuclear physicists and astrophysicists reported here has been made possible through the contract ERBCHRXCT930339 of the European Commission.

## References

[1] S. Goriely, A. Jorissen, M. Arnould, Proc. Fifth Workshop on nuclear astrophysics, eds. W. Hillebrandt and E. Müller, Max Planck Inst. für Astrophys. Rep. (1989) p. 60.

[2] S.E. Woosley, 1986, 16th Saas-Fee course, Nucleosynthesis and Chemical Evolution., eds. J. Audouze, C. Chiosi, S.E. Woosley, Geneva Observ., p. 1.

[3] M. Politano, S. Starrfield, J.W. Truran, A. Weiss and W.M. Sparks, Astrophys. J. 448 (1995) 807.

[4] A. Coc, R. Mochkovitch, Y. Oberto, J.-P. Thibaud and E. Vangioni-Flam, Astron. Astrophys. 299 (1995) 479.

[5] S.E. Woosley and W.C. Haxton, Nature 334 (1988) 45.

[6] S.E. Woosley, D.H. Hartmann, R.D. Hoffman and W.C. Haxton, Astrophys. J. 356 (1990) 272.

[7] W.C. Haxton, Proc. Int. Workshop on Unstable Nuclei in Astrophysics, eds. S. Kubono and T. Kajino (World Scientific, Tokyo, 1991) p. 263.

[8] G. Meynet and M. Arnould, Nuclei in the Cosmos, Proc. 2nd Int. Symp. on nuclear astrophysics held at Karlsruhe, Germany, 6-10 July, 1992 (Institute of Physics Publishing Bristol and Philadelphia) p. 503.

[9] M. Forestini, S. Goriely, A. Jorissen and M. Arnould, Astron. Astrophys. 261 (1992) 157.

[10] A. Jorissen, V.V. Smith and D.L. Lambert, Astron. Astrophys. 261 (1992) 164.

[11] G.R. Caughlan and W.A. Fowler (CF88), At. Data Nucl. Data Tables 40 (1988) 283.

[12] D.W.O. Rogers, A.L. Carter, T.J.M. Symons, S.P. Dolan, N. Anyas-Weiss and K.W. Allen, Can. J. Phys. 54 (1976) 938.

[13] R. Middleton, Proc. Int. Conf. on Nuclear Reaction Induced by Heavy Ions, eds. R. Bock and W.R. Hering (North-Holland, 1970) p. 263.

[14] K.I. Kubo, Nucl. Phys. A 187 (1972) 205.

[15] F. de Oliveira, Thesis, Orsay, France, (1995) unpublished.

[16] F. Ajzenberg-Selove, Nucl. Phys. A 475 (1987) 1.

[17] C.L. Woods, B.A. Brown and N.A. Jelley, J. Phys. G 8 (1982) 1699.

[18] F.D. Becchetti, E.R. Flynn, D.L. Hanson and J.W. Sunier Nucl. Phys. A 305 (1978) 293.

[19] M.E. Cobern, D.J. Pisano and P.D. Parker. Phys. Rev. C 14 (1976) 491.

[20] K.I. Kubo, F. Nemoto and H. Bando, Nucl. Phys. A 224 (1974) 573.

[21] M.H. Macfarlane and S. Pieper, Argonne-Indiana-Stonybrook direct reaction program PTOLEMY March 1983 version, Argonne National Laboratory, ANL-76-11, Internal report.

[22] P.D. Kunz, DWUCK5-distorted waves, U. Colorado, 30/jun/1982 version, private communication.

[23] G.R. Satchler, Direct Nuclear Reactions, Oxford Science Publications (1983), and references therein.

[24] K.I. Kubo and M. Hirata, Nucl. Phys. A 187 (1972) 186.

[25] I. Tserruya, B. Rosner and K. Bethge, Nucl. Phys. A 213 (1973) 22.

[26] H.T. Fortune and D. Kurath. Phys. Rev. C 18 (1978) 236.

[27] B. Buck and A.A. Pilt, Nucl. Phys. A 280 (1977) 133.

[28] H.T. Fortune, J. Phys. G 5 (1979) 381.

[29] F.D. Becchetti and G.W. Greenless, in: Polarization Phenomena in Nuclear Reactions, H.H. Barshall and W. Haeberli, eds. (The University of Madison Press, Madison, 1971) p. 682.

[30] J.N. Blatt and V.F. Weiskopf, Theoretical Nuclear Physics (Wiley, New York, 1963) p. 420.

[31] R.P. Ward and P.R. Hayes, At. Data Nucl. Data Tables 49 (1991) 315.

[32] J. Vernotte, G. Berrier-Ronsin, J. Kalifa and R. Tamisier, Nucl. Phys. A 390 (1982) 285.

[33] M. Mermaz, Thesis, 1967, Université de Paris, CEA-R3078 internal report, unpublished.

[34] D.W.O. Rogers, J.H. Aitken and A.E. Litherland, Can. J. Phys. 50 (1972) 268.

[35] P.V. Magnus, M.S. Smith, P.D. Parker, R.E. Azuma, C. Campbell, J.D. King and J. Vise, Nucl. Phys. A 470 (1987) 206.

[36] F. Ajzenberg-Selove, Nucl. Phys. A 190 (1972) 1.

[37] P.V. Magnus, M.S. Smith, A.J. Howard and P.D. Parker, Nucl. Phys. A 506 (1990) 332.

[38] W.A. Fowler, G.R. Caughlan and B.A. Zimmerman, Ann. Rev. Astron. Astrophys. 13 (1975) 69.

[39] P. Descouvemont, 1995, private communication.

[40] N. Mowlavi, A. Jorissen and M. Arnould, 1995, submitted to Astron. Astrophys.

[41] N. Mowlavi, 1995, Ph.D. thesis, Université Libre de Bruxelles (Belgium).